

Joint Reconstruction in Low Dose Multi-Energy CT

Jussi Toivanen^{*}, Alexander Meaney^{**}, Samuli Siltanen^{**} and Ville Kolehmainen^{*}

^{*}Department of Applied Physics, University of Eastern Finland,
POB 1627, FI-70211 Kuopio, Finland

^{**}Department of Mathematics and Statistics, University of
Helsinki, Finland

December 15, 2024

Abstract

Multi-energy CT takes advantage of the non-linearly varying attenuation properties of elemental media with respect to energy, enabling more precise material identification than single-energy CT. The increased precision comes with the cost of a higher radiation dose. A straightforward way to lower the dose is to reduce the number of projections per energy, but this makes tomographic reconstruction more ill-posed. In this paper, we propose how this problem can be overcome with a combination of a regularization method that promotes structural similarity between images at different energies and a suitably selected low-dose data acquisition protocol using non-overlapping projections. The performance of various joint regularization models is assessed with both simulated and experimental data, using the novel low-dose data acquisition protocol. Two of the models are well-established, namely the joint total variation and linear parallel level sets regularization. Furthermore, two new joint regularization models are introduced for multi-energy CT: one is a spectral smoothness promoting regularizer and the other a regularizer based on the structure function from the structural similarity index. The findings show that joint regularization outperforms individual channel-by-channel reconstruction. Furthermore, the proposed combination of joint reconstruction and non-overlapping projection geometry enables significant reduction of radiation dose.

1 Introduction

Computed tomography (CT) is an imaging modality in which the interior structure of an object is reconstructed from X-ray transmission images recorded along different directions. The reconstructed object is typically presented as cross-sectional images or 3D volumetric data. CT imaging plays an ever-diversifying role in medical imaging and industrial applications, with continuing methodological developments being motivated by the desire for increased image quality and information, and for reductions in radiation dose [1, 2]. Advances in CT imaging have been driven both by hardware improvements, such as better detectors and X-ray tubes, and by algorithmic developments in reconstruction methods [3, 4].

A CT image is a greyscale image where the value of a pixel or voxel in a given location is proportional to the X-ray attenuation coefficient of the medium in the corresponding location. A significant limitation of conventional CT imaging is that no bijective relationship exists between the reconstructed greyscale value and the material properties, *i.e.*, elemental composition and mass density. Therefore, two tissues of entirely differing properties may be reconstructed as the same value, a typical example being bone and iodine contrast agent [5]. More information on the material composition can be obtained by using dual- or multi-energy CT imaging, where the object is imaged using more than one X-ray energy, and the non-linearly varying attenuation properties of different elemental media are exploited for material identification [1, 5]. Applications of multi-energy CT, also known as spectral CT, include differentiation and quantification of materials, tissue characterization, virtual monoenergetic imaging, automated bone removal in CT angiography, cardiovascular imaging, multiple contrast agent imaging, and mapping of effective atomic number [5, 6, 7, 8, 9, 10, 11, 12, 13, 14, 15, 16, 17].

Multi-energy CT imaging was first proposed in the 1970s [18], and today there exist many data acquisition schemes for spectral X-ray imaging: sequential scanning, rapid tube voltage switching, dual source scanning, multilayer detectors, and photon-counting detectors [5]. Compared to traditional radiography, CT is a high-dose modality [19]. Although the risks of radiation doses in the range of a few millisieverts remains a controversial topic [20, 21], an underlying philosophy in CT development is to reduce the dose as much as possible, in accordance with the ALARA (As Low As Reasonably Achievable) principle [22, 23]. There is a concerted effort to push the radiation dose from routine CT examinations to less than 1 millisievert, which is well below the annual dose due to background radiation [3]. Both image quality and radiation dose depend fundamentally on the number of photons used in imaging, and an acceptable balance needs to be found between the two factors [24]. Radiation dose can be reduced by reducing the number of photons used, and one efficient way of achieving this is to reduce the number of X-ray projections [3, 25, 26]. However, image reconstruction from sparse projections requires algorithms more advanced than the standard approach where attenuation at each measured energy is reconstructed independently using classical techniques, such as the filtered

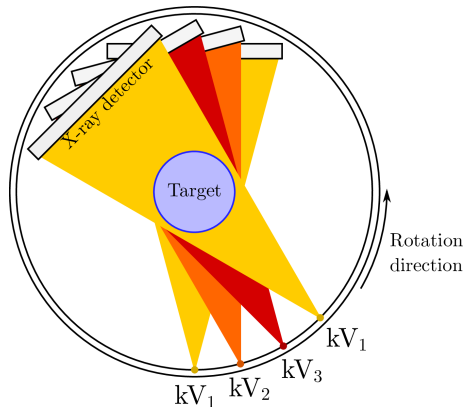


Figure 1: Illustration of a spectrally non-overlapping projection sampling scheme for low dose multi-energy CT imaging. The X-ray source energies $E_k, k = 1, 2, 3$ are denoted by tube voltages kV_1, kV_2, kV_3 .

backprojection (FBP) algorithm.

A highly feasible approach for low dose multi-energy CT is to utilize a multi-channel joint reconstruction approach where all the unknown images are reconstructed simultaneously by solving one combined inverse problem. The central idea is to combine all the projection data into a single image reconstruction problem and to utilize regularization models that promote some prior information on the unknown images within and across the energies. In multi-energy CT, a reasonable prior assumption for the attenuation images at different energies is that they can be expected to be *structurally* similar in the sense that an edge (e.g. an organ boundary) that is present at one energy, is likely to be at same location and alignment with the other energies as well, even though the contrast between materials will be different at each energy. There are many algorithms in the literature designed for promoting structural similarity. These include vectorial total variation [27, 28], spectral patch-based penalty for the maximum likelihood method [29], tensor-based dictionary learning [30, 31], parallel level sets [32], the prior rank, intensity and sparsity model (PRISM) [33, 34], tensor-based nuclear norm regularization [35], nonlocal low-rank and sparse matrix decomposition [36], and total variation regularization using non-convex optimization [37].

In this paper, we study the performance of various structural similarity promoting joint reconstruction models using a novel low dose data acquisition protocol. We consider two well established models: joint total variation [38] and linear parallel level sets [39]. Furthermore, we introduce two new joint regularization models for multi-energy CT. One is a spectral smoothness regularization promoting continuity of the attenuation coefficient in the energy dimension, and the other is a joint regularization model based on the structural similarity index [40].

We combine the joint reconstruction approaches with a novel low-dose data acquisition protocol. We collect data using a sparse angular sampling, using a different X-ray energy in consecutive steps. See Figure 1 for an illustration. For example with three different energies this protocol drops the radiation dose down to one third compared to the option of measuring all energies at all angles.

The attenuation images at different energies are structurally similar. Therefore, the combination of non-overlapping sampling and joint regularization model should not compromise image quality. In this paper, the proposed combination of joint reconstruction and non-overlapping sampling is evaluated with simulated multi-energy CT data and experimental data from a biological specimen.

The rest of this paper is organized as follows. The forward modeling of multi-energy CT is explained in Section 2 and the reconstruction methods used in this paper in Section 3. The generation of simulated data and measuring of the experimental data are explained in Section 4. The results with simulated and experimental measurement data are shown and discussed in Section 5. Section 6 gives the conclusions.

2 Forward Problem for Multi-Energy CT

In multi-energy CT, X-ray images of an object are acquired at two or more X-ray energies to obtain information on the energy-dependent attenuation properties of the object for differentiation and identification of materials. Multiple acquisition schemes exist for obtaining spectral CT data, detailed in, *e.g.*, [5]. Regardless of how the multi-energy data is acquired, the forward model for multi-energy CT is typically based on the linear projection model of conventional CT.

To define our forward model, we consider a multi-energy CT experiment with n X-ray energies $\{E_k, k = 1, \dots, n\}$. Let Ω denote the image domain (2D area or 3D volume) and $\mu(r, E_k) : \Omega \mapsto \mathbb{R}_+$ denote the attenuation function for energy E_k with X-ray source intensity $I_0(E_k)$ where r are the spatial coordinates. With these notations, the X-ray intensity at a detector element placed behind the object is modelled by the Beer-Lambert law:

$$I = I_0(E_k) e^{-\int_{\text{ray}} \mu(r, E_k) ds}, \quad (1)$$

where the integration path is along the straight ray from the X-ray source to the detector element [24]. By normalizing with the source intensity and taking the logarithm, we obtain the conventional linear attenuation model

$$\int_{\text{ray}} \mu(r, E_k) ds = -\ln \frac{I}{I_0(E_k)}. \quad (2)$$

We remark that the linear attenuation model (2) is based on several physical approximations, namely neglecting any scattering effects and the energy dependencies of the attenuation coefficients across the X-ray spectrum for polychromatic sources. Taking all these factors into account would lead to integro-differential light transport models, which would be computationally infeasible.

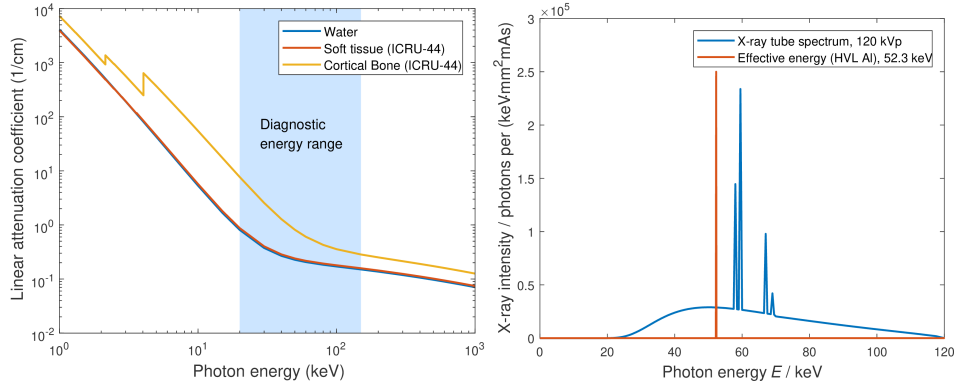


Figure 2: Left: The X-ray attenuation coefficients of water, soft tissue, and cortical bone as functions of X-ray energy. The raw data was obtained from NIST [42]. Right: Example of a realistic tungsten X-ray source spectrum with 120 kVp voltage and filtering (2.5 mm Al + 0.2 mm Cu), and monochromatic radiation with the same effective energy. The spectra were computed using the SpekCalc software [43].

Figure 2 shows on the left examples of the energy-dependencies of the X-ray coefficients of three materials of medical relevance, and on the right a realistic example of an energy spectrum of an X-ray source. In principle, when only the scattering effects are neglected, an energy dependent ray propagation based attenuation model would be

$$I = \int_0^{E_{\max}} I_0(E) e^{-\int_{\text{ray}} \mu(r, E) ds} dE. \quad (3)$$

where E_{\max} is the maximum energy in the X-ray source spectrum, leading to a non-linear problem for the X-ray tomography. While the non-linear model could in principle be used, it would require accurate knowledge of the input spectrum $I_0(E)$ and either a large number of different measured energies (input spectra) or a spectrally resolved measurement in an attempt to recover $\mu(r, E)$ with a high energy resolution. In practice, however, the projection measurements are typically taken only with a few energies (X-ray spectra) and the measurement for each energy is approximated by the linear model (2) where E_k is thought of as an effective energy for the respective X-ray source spectrum. The effective energy of a polychromatic source is defined as the energy of a monochromatic beam that has the same half-value layer (HVL) as the polychromatic x-ray beam in a given material, usually aluminum or copper [41]. The use of the linear approximation, however, often results in problems in image reconstruction, such as beam-hardening and metal artifacts [24].

For a computational implementation the forward model (2) that we use must be appropriately discretized. By concatenating all the X-ray projection

data that is measured for the (effective) energy E_k into a vector $y_k \in \mathbb{R}^{M_k}$, the forward model for the projection data becomes

$$y_k = A_k x_k + e_k \quad (4)$$

where $x_k \in \mathbb{R}^N$ is the vectorized representation of the (spatial) discretization of the unknown attenuation image $\mu(r, E_k)$ with energy E_k , e_k models the measurement noise, and A_k is the matrix which implements the discretization of the projection model (2) for the particular projection geometry and projection angles used with energy E_k . The whole multi-energy CT experiment consist of a set $\{y_k, k = 1, \dots, n\}$ data vectors of the form (4).

We remark that the number M_k of data points for different energies in the joint reconstruction can be freely chosen and could be different for each measured energy (*e.g.* using fewer measurements for the higher energies).

3 Inverse Problem in Multi-Energy CT

In this section, we discuss the joint reconstruction approach and the joint regularization models that are employed in this study. However, first we will briefly review unregularized reconstruction and total variation (TV) regularized reconstruction for (single energy) CT since they will be employed as references for the joint reconstructions in the numerical examples.

3.1 Least Squares (LS) Reconstruction

When densely collected projection data for each energy is available, the image reconstructions are typically carried out by using classical methods such as the filtered backprojection (FBP) [44], Kaczmarz iterations such as the algebraic reconstruction technique (ART) [44], or iterative techniques which minimize the least squares (LS) data misfit

$$F(x_k) = \|y_k - A_k x_k\|^2 \quad (\text{No prior}) \quad (5)$$

where y_k is the projection data (using single energy k), A_k is the system matrix (or projection matrix) and x_k is the unknown (vectorized) image.

In this paper, the LS estimate is used as one reference estimate for the joint reconstruction, giving a reference of an estimate which is obtained from the given data y_k without prior information.

3.2 Sparsity Promoting Reconstruction in CT

The ALARA principle for X-ray dose in CT imaging has led to significant efforts in development of reconstruction methods that can provide high quality reconstructions from sparsely collected projection data. In the spirit of the theory of compressed sensing [45], the methods are usually based on some type of regularization which promotes sparsity of the unknown image by an l_1 norm

regularization functional on the image on some domain. The l_1 regularization can be based, for example, on wavelets [26], shearlets [46], or the total variation (TV) which promotes piecewise regular solutions by posing the l_1 regularization for the gradient of the unknown image [47, 48, 49, 50].

Using the framework of regularized least squares minimization, the TV regularized reconstruction can be stated as minimization of the objective functional

$$F(x_k) = \|y_k - A_k x_k\|^2 + \gamma_k TV(x_k) \quad (\mathbf{TV}) \quad (6)$$

where

$$TV(x_k) = \int_{\Omega} (\|\nabla x_k\|^2 + \beta^2)^{1/2} dr \quad (7)$$

is the (smooth) total variation functional [51], $\beta > 0$ is a smoothing parameter, $\gamma_k > 0$ is a regularization parameter, and r is the spatial coordinate vector.

In multi-energy CT, one can reconstruct the images at different energies using the TV regularization separately for each energy. In this paper, this approach is used as the other reference for the joint reconstructions, giving a reference of sparsity promoting reconstructions which are computed independently for each energy without any prior model for the correlation of the images between the energies.

3.3 Joint Reconstruction in Multi-Energy CT

In joint reconstruction, the central idea is to combine all the data sets $\{y_1, \dots, y_n\}$, where n is the number of energies, together with a joint regularization functional into a single problem of reconstructing all the unknown images $\{x_1, x_2, \dots, x_n\}$ at once. In the regularized least squares framework, the objective functional for the joint reconstruction can be stated as

$$F(x_1, \dots, x_n) = \sum_{k=1}^n \|y_k - A_k x_k\|^2 + R(x_1, x_2, \dots, x_n) \quad (8)$$

where y_k is the measurement vector and A_k is the system matrix corresponding to energy k , and

$$R(x_1, x_2, \dots, x_n) = \sum_{k=1}^n \gamma_k U(x_k) + \alpha W(x_1, x_2, \dots, x_n) \quad (9)$$

is the regularization functional where $U(x_k)$ is a (spatial) regularization functional acting separately on each of the images x_k , $W(x_1, x_2, \dots, x_n)$ is a joint regularization functional which is used to incorporate prior information across the different energies, and γ_k and α are regularization parameters.

The regularization functional $W(x_1, x_2, \dots, x_n)$ should be formulated to promote feasible *a priori* information between the unknown images at different energies. In multi-energy CT, it is reasonable to assume that the attenuation

images at different energies are structurally similar in the sense that if an edge is present with one energy, it is likely to be at the same location and alignment with other energies as well.

The following subsections introduce the joint regularization functionals used in this paper.

3.3.1 Joint Total Variation

The joint total variation (JTV) functional was originally developed for denoising and deblurring of the red, green, and blue channels in RGB images [38]. It can be defined as

$$JTV(x_1, x_2, \dots, x_n) = \int_{\Omega} (||\nabla x_1||^2 + ||\nabla x_2||^2 + \dots + ||\nabla x_n||^2 + \beta^2)^{1/2} dr \quad (10)$$

and it promotes sparsity of the joint gradient, leading to edge preserving regularization within each image and favoring the locations of edges to be the same in the images x_k .

In the JTV regularization, we set $U(x_i) = 0$ and $W(x_1, x_2, \dots, x_n) = JTV(x_1, x_2, \dots, x_n)$ in (9), leading to

$$R(x_1, x_2, \dots, x_n) = \alpha JTV(x_1, x_2, \dots, x_n) \quad (\mathbf{JTV}) \quad (11)$$

in (8).

3.3.2 Linear Parallel Level Sets

The linear parallel level sets (LPLS) prior was originally used for denoising and demosaicking RGB images [39]. In tomographic context, it has been used in joint reconstruction of PET and MRI images [52], reconstruction of PET images with MRI images as side information [53] and in multi-energy computed tomography [32].

The LPLS prior is based on the idea that level sets can be used to identify the structure in images and that the gradients of an image are always perpendicular to the level sets. Therefore, structural similarity can be measured by measuring the parallelism of the gradients' orientations in two images. In the context of a minimization problem, this can be formulated as [53]

$$LPLS(x_k, x_j) = \int_{\Omega} \left((||\nabla x_k||^2 + \beta^2)^{1/2} (||\nabla x_j||^2 + \beta^2)^{1/2} - (|\langle \nabla x_k, \nabla x_j \rangle|^2 + \beta^4)^{1/2} \right) dr \quad (12)$$

and in this paper, the computation is done in pairs, so that

$$LPLS(x_1, x_2, \dots, x_n) = LPLS(x_1, x_2) + LPLS(x_2, x_3) + \dots + LPLS(x_n, x_1). \quad (13)$$

In the LPLS regularization, we set $U(x_i) = 0$ and $W(x_1, x_2, \dots, x_n) = LPLS(x_1, x_2, \dots, x_n)$ in (9), leading to the regularization functional

$$R(x_1, x_2, \dots, x_n) = \alpha LPLS(x_1, x_2, \dots, x_n) \quad \textbf{(LPLS)} \quad (14)$$

3.3.3 Spectral Smoothness Regularization

A straightforward way to promote structural similarity is to use smoothness regularization in the spectral (energy) dimension. Spectral smoothness regularization can be obtained simply by penalizing differences between the images $\{x_k\}$. In this paper, we consider a spectral smoothness regularization term based on the first finite difference but also higher order finite differences could be used.

The first finite difference can be used for regularization with

$$D1(x_k, x_{k+1}) = w_k \int_{\Omega} ||x_{k+1} - x_k||^2 dr \quad (15)$$

and it favors images that are close to being identical. The parameter w_k in (15) basically corresponds to the reciprocal of the (spectral) distance (energy difference) between the images x_{k+1} and x_k . However, in cases where one might have prior information about the spatial variations in the expected magnitudes of the changes between the images x_{k+1} and x_k , the parameter w_k could be made spatially distributed for construction of a spatially weighted regularization model for the spectral smoothness. For more than two images x_i we can write

$$D1(x_1, x_2, \dots, x_n) = D1(x_1, x_2) + D1(x_2, x_3) + \dots + D1(x_{n-1}, x_n). \quad (16)$$

In this paper, we set the weights $w_k \equiv 1$, and use the regularization functional

$$R(x_1, x_2, \dots, x_n) = \alpha D1(x_1, x_2, \dots, x_n) \quad \textbf{(D1)} \quad (17)$$

for D1 regularization.

Notice that the D1 regularizer imposes a penalty only for the differences of the pixel values in the energy direction. When using highly sparse projection data, this lack of spatial constraint can result in spatially noisy images. In such cases, an additional spatial regularization term, such as total variation (7), can be used to promote regularity within each of the images. This can be done by choosing $U(x_i) = TV(x_i)$ in (9), leading to

$$R(x_1, x_2, \dots, x_n) = \sum_{k=1}^n \gamma_k TV(x_k) + \alpha D1(x_1, x_2, \dots, x_n) \quad \textbf{(D1+TV)} \quad (18)$$

for the D1+TV regularization.

3.3.4 Structural Similarity Index Based Regularization

A new joint regularization model which favors structural similarity can be formulated by considering the structural similarity (SSIM) index [40, 54] which is

an image metric that assesses the similarity of two images by using three characteristics of the input images: luminance, contrast, and structure. Here we consider only the structure part which associates the unit vectors $(x_1 - \mu_{x_1})/\sigma_{x_1}$ and $(x_2 - \mu_{x_2})/\sigma_{x_2}$ with the structure of the two images and uses their inner product to measure the structural similarity, resulting in

$$\hat{S}(x_1, x_2) = \frac{\sigma_{x_1 x_2} + C}{\sigma_{x_1} \sigma_{x_2} + C} \quad (19)$$

where $\sigma_{x_1 x_2}$ is the cross correlation, σ_{x_1} and σ_{x_2} are the standard deviations, and μ_{x_1} and μ_{x_2} are the expected values of x_1 and x_2 , and C is a small constant introduced to avoid division by zero. Geometrically, the cross correlation $\sigma_{x_1 x_2}$ corresponds to the cosine of the angle between the vectors $x_1 - \mu_{x_1}$ and $x_2 - \mu_{x_2}$, and thus (19) is maximized when these vectors point in the same direction and minimized when they point in opposite directions.

As with the SSIM index, it is possible to compute an image showing the similarity in structure of two images. Following the procedure for computing a SSIM map [40], but only for the structure part (19), the cross correlations and standard deviations, as well as \hat{S} itself, are computed locally using a 11x11 window that moves pixel by pixel over the entire image. If we let \mathcal{N}_i denote the set of indices for the 11x11 window for pixel i in the image lattice, and let $w = \{w_k | k \in \mathcal{N}_i\}$ denote the local weights obtained from a circular symmetric Gaussian weighting function with standard deviation of 1.5, local weighted statistics for window i can be computed as

$$(\sigma_{x_k})_i = \left(\sum_{j \in \mathcal{N}_i} w_j ((x_k)_j - \mu_{x_k})^2 \right)^{\frac{1}{2}} \quad (20)$$

$$(\mu_{x_k})_i = \sum_{j \in \mathcal{N}_i} w_j (x_k)_j \quad (21)$$

$$(\sigma_{x_k x_p})_i = \sum_{j \in \mathcal{N}_i} w_j ((x_k)_j - \mu_{x_k}) ((x_p)_j - \mu_{x_p}) \quad (22)$$

where $(x_k)_j$ is the j th element of x_k . The obtained pixel-by-pixel local \hat{S} form the structural similarity map with larger values indicating similarity and smaller values indicating structural differences. Now we can use the mean of the local \hat{S} values

$$\bar{S}(x_k, x_p) = \frac{1}{N} \sum_{i=1}^N (\hat{S}(x_k, x_p))_i \quad (23)$$

where N is the number of pixels in the images and $(\hat{S}(x_k, x_p))_i$ is the value of \hat{S} in pixel i , as a scalar measure of the structural similarity which is maximized with the value 1 when the images x_k and x_p are identical. Now the regularization term in (8) can be chosen to be some decreasing function of all the $\bar{S}(x_k, x_{k+1})$

which has minimum when the image pairs are identical. In this paper, we use a simple choice

$$S(x_1, x_2, \dots, x_n) = \frac{1}{\bar{S}(x_1, x_2, \dots, x_n)} \quad (24)$$

where

$$\bar{S}(x_1, x_2, \dots, x_n) = \bar{S}(x_1, x_2) + \bar{S}(x_2, x_3) + \dots + \bar{S}(x_n, x_1) \quad (25)$$

computes the structure parts in pairs.

When employing the structural similarity regularization alone, we set $U(x_i) = 0$ and use

$$R(x_1, x_2, \dots, x_n) = \alpha S(x_1, x_2, \dots, x_n) \quad (\mathbf{S}) \quad (26)$$

as the regularization functional in (8) for S regularization.

Similarly as with the spectral smoothness regularization, the lack of penalty for spatial regularity within each channel in the structural regularization term (24) can result in spatially noisy reconstructions when using sparse projection data. In such cases, an additional spatial regularization term, such as total variation (7), can be used to promote spatial regularity of the reconstructions. In this paper, we use $U(x_i) = TV(x_i)$ in (9), leading to

$$R(x_1, x_2, \dots, x_n) = \sum_{k=1}^n \gamma_k TV(x_k) + \alpha S(x_1, x_2, \dots, x_n) \quad (\mathbf{S+TV}) \quad (27)$$

for the S+TV regularization.

4 Materials and Methods

In this section, we present the simulated and measured X-ray projection data that were used to test the different regularization models utilized in multi-energy CT reconstruction. The datasets were generated using dense angle sampling, and could then later be appropriately subsampled to simulate sparse-angle acquisition schemes.

4.1 Simulated Data

Simulated X-ray projection data was generated using idealized, monochromatic sources in a parallel beam geometry. For this, a computational anthropomorphic 2D phantom was created using the XCAT software [55, 56]. The phantom consisted of a single cross-sectional slice of an adult human male chest. A calcified coronary artery was placed in the heart of the phantom. We simulated three sets of noise-free projections using 40 keV, 80 keV, and 120 keV X-rays. Each set consisted of 360 projections taken evenly across 180° at 0.5° intervals. The X-ray detector was a line detector consisting of 729 elements, with a pixel

Table 1: Imaging geometry used for collecting the experimental data.

Parameter	Value
Focus-center distance	252 mm
Focus-detector distance	420 mm
Magnification	5/2
Detector pixel size	0.200 mm
Effective pixel size	0.120 mm
Projection size	552×576 pixels
Angular range	360°
#projections	720

size of 0.875 mm. To avoid committing inverse crime, the projections were generated using XCAT’s own CT Projector tool.

The noisy realizations of the simulated measurements for each energy were obtained by adding Gaussian zero mean random noise with standard deviation equal to one percent of the maximum amplitude of the measurements with that energy to the simulated noise-free measurements.

The reconstruction grid size was 512×512 pixels. The forward operators for the model $Ax_k = y_k$ were created using the ASTRA Toolbox [57, 58, 59].

4.2 Experimental Data

Experimental data was gathered at the Department of Physics, University of Helsinki, using a cone-beam micro-CT scanner with an end-window tube and a tungsten target (GE Phoenix nanotom 180 NF). The chest of a small bird (the common quail, *Coturnix coturnix*) was used as a test phantom, as it contains multiple different tissue types as well as fine details arising from the bone structure. The bird phantom was imaged using three different X-ray tube settings in the same geometry. Multiple frames were averaged for each projection in order to increase signal-to-noise ratio. The imaging geometry is specified in Table 1 and the settings for each effective energy are specified in Table 2. 2D sinograms were created using the central plane of the cone-beam projections, in which the geometry reduces to a fan-beam geometry.

The reconstruction grid size was 512×512 pixels with a pixel size of 120 μm , and the forward operators for the imaging model were created using the ASTRA Toolbox.

4.3 Image Fidelity Measures

To quantify the quality of reconstructions in the simulation test case, we use the root mean square error (RMSE) and the mean structural similarity (MSSIM) index [40].

Table 2: Energy-specific settings used for collecting the experimental data.

Energy	U (kV)	Filtration	I (μA)	Exposure time (ms)	Frame averaging
E_1	50	None	300	125	4
E_2	80	1 mm Al	180	125	4
E_3	120	0.5 mm Cu	120	250	4

The root mean square error can be written as

$$\text{RMSE}(x_k) = \sqrt{\frac{1}{N} \sum_{i=1}^N ((x_k)_i - (x_{\text{REF},k})_i)^2} \quad (28)$$

where $(x_k)_i$ denotes the i th pixel of the solution x corresponding to energy k and $x_{\text{REF},k}$ is the reference image corresponding to energy k .

The structural similarity (SSIM) index [40] aims to measure the perceived similarity in two images, x_1 and x_2 . It assesses the luminance $l(x_1, x_2)$, contrast $c(x_1, x_2)$ and structure $s(x_1, x_2)$ and can be written as

$$\begin{aligned} \text{SSIM} &= l(x_1, x_2)c(x_1, x_2)s(x_1, x_2) \\ &= \left(\frac{2\mu_{x_1}\mu_{x_2} + C_1}{\mu_{x_1}^2 + \mu_{x_2}^2 + C_1} \right) \left(\frac{2\sigma_{x_1}\sigma_{x_2} + C_2}{\sigma_{x_1}^2 + \sigma_{x_2}^2 + C_2} \right) \left(\frac{\sigma_{x_1x_2} + C_3}{\sigma_{x_1}\sigma_{x_2} + C_3} \right) \end{aligned} \quad (29)$$

where μ is the mean, σ is the standard deviation, $\sigma_{x_1x_2}$ is the cross-correlation and C_1 , C_2 and C_3 are small constants used to avoid division by zero. The mean SSIM index is obtained by first computing the SSIM index locally for each pixel using a 11x11 pixel window whilst also using a Gaussian weighting function for the statistics, as in (20 – 22), and then the final index is obtained as the mean of these local SSIM indices. For a reconstructed image x_k and a reference image $x_{\text{REF},k}$, this can be written as

$$\text{MSSIM}(x_k, x_{\text{REF},k}) = \frac{1}{N} \sum_{i=1}^N (\text{SSIM}(x_k, x_{\text{REF},k}))_i \quad (30)$$

where $(\text{SSIM}(x_k, x_{\text{REF},k}))_i$ is the local value of SSIM for pixel i in the image lattice.

As the anthropomorphic XCAT target phantom that was used as the basis for the projection data does not translate well into attenuation images that could be used as ground truth reference images, the ground truth reference images $x_{\text{REF},k}$ for the simulation test case were obtained by computing full *noiseless data* (360 angles for each energy) filtered backprojection (FPB) reconstructions using the ASTRA Toolbox [57, 58, 59] FBP algorithm.

For the test case with experimental data, the reference images $x_{\text{REF},k}$ were obtained by the 'No Prior' method in (5) applied to 720 projections for each measured energy.

4.4 Selection of the Regularization Parameters γ_k and α

For the simulation test case, the regularization parameters γ_k and α in (6) and (8) for each regularization term were selected by computing a series of reconstructions with varying γ_k and α . Then the mean structural similarity index (30) was computed for each reconstructed image using the full data FPB reconstructions as the reference images $x_{\text{REF},i}$, and the γ_k and α corresponding to the highest structural similarity were selected for the test cases. A similar procedure was used in the experimental data test case but the identification of best reconstructions was done with visual comparison. The selected γ_k and α for each regularization term are given in Table 3.

Table 3: Selected α and γ_k parameters for the different regularization terms for the simulated data test case ($\alpha_{\text{SIM}}, \gamma_{k,\text{SIM}}$) and for the experimental data test case ($\alpha_{\text{EXP}}, \gamma_{k,\text{EXP}}$). The three values of γ_k are for the three different tube energies with indices $k = 1, 2, 3$.

Prior	Acronym	α_{SIM}	$\gamma_{k,\text{SIM}}$	α_{EXP}	$\gamma_{k,\text{EXP}}$
No prior	No prior	-	-	-	-
Total variation	TV	-	2.25, 0.8, 0.7	-	1.0, 0.5, 0.25
Joint total variation	JTV	2.25	0	1	0
Linear parallel level sets	LPLS	4000	0	6000	0
First difference	D1	400	0	100	0
Structural	S	4e6	0	1e6	0
First difference + TV	D1+TV	50	1.125, 0.4, 0.35	70	0.5, 0.25, 0.125
Structural + TV	S+TV	0.75e5	1.125, 0.4, 0.35	0.5e6	0.5, 0.25, 0.125

5 Results and Discussion

In this section, reconstructions computed using the joint reconstruction approaches in Section 3.3 are presented and compared to the full data reference images and to the single-energy reference methods (5) (no prior) and (6) (TV) where attenuation at each energy is reconstructed separately. The first subsection introduces the multi-energy projection geometry, the second subsection shows results computed with simulated data and the third subsection shows results computed with experimental measurement data.

For both simulated and experimental data test cases, (5), (6) and (8) were minimized using a Polak-Ribière nonlinear conjugate gradient method [60] with a golden section line search and a non-negativity constraint.

5.1 Multi-Energy Projection Geometry

The principle of the low dose multi-energy projection geometry is illustrated in Figure 1 for an experiment with three different energies, denoted by the X-ray tube voltages kV_1 , kV_2 and kV_3 in the picture. Instead of sampling all the projection directions with all the energies, the directions are divided to non-overlapping sets of interleaved projection directions making the projection geometry different for each of the used source energies. This type of imaging setup could be realistically implemented in a clinical CT scanner using a rapid-kVp switching scheme.

In this study, the non-overlapping low dose data sets were obtained by retrospective subsampling of the full angle data sets with three different source energies. In both the simulation and experimental data cases, a subset of 90 equally spaced projection angles were chosen from the whole angular span of the projection geometry. This subset was then further subsampled to three subsets of 30 angles, leading to 30 equally spaced projection directions for each energy, see Figure 1 and Table 4. For each energy, the projection data corresponding to the set of 30 angles was used in the computations.

Table 4: Measurement angles used for energies E_1 , E_2 and E_3 in the simulated data case (left) and experimental data case (right).

E_1	E_2	E_3	E_1	E_2	E_3
0	2	4	0	4	8
6	8	10	12	16	20
12	14	16	24	28	32
\vdots	\vdots	\vdots	\vdots	\vdots	\vdots
162	164	166	324	328	332
168	170	172	336	340	344
174	176	178	348	352	356

5.2 Simulated Data

The reconstructed images for the simulated data test case are shown in Figure 3. The first three columns show the reconstructions for energies 40, 80 and 120 keV, respectively, and the next three columns show a region of interest from the corresponding reconstructions. Figure 4 shows the RMSE and MSSIM fidelity metrics for the reconstructions.

All the joint reconstructions (JTV, LPLS, D1, S, D1+TV, S+TV) in Figure 3 are visually better than the independent single energy reconstructions (No prior, TV) in the sense that more of the details that are present in the full data reference images can be detected in the reconstructions. This could be expected since the sub-problems with different energies and projection directions are coupled to each other in the joint reconstruction approaches via the joint regularization functional. The (S+TV) reconstructions have the best fidelity in the RMSE measure and the (LPLS) reconstructions in the MSSIM measure,

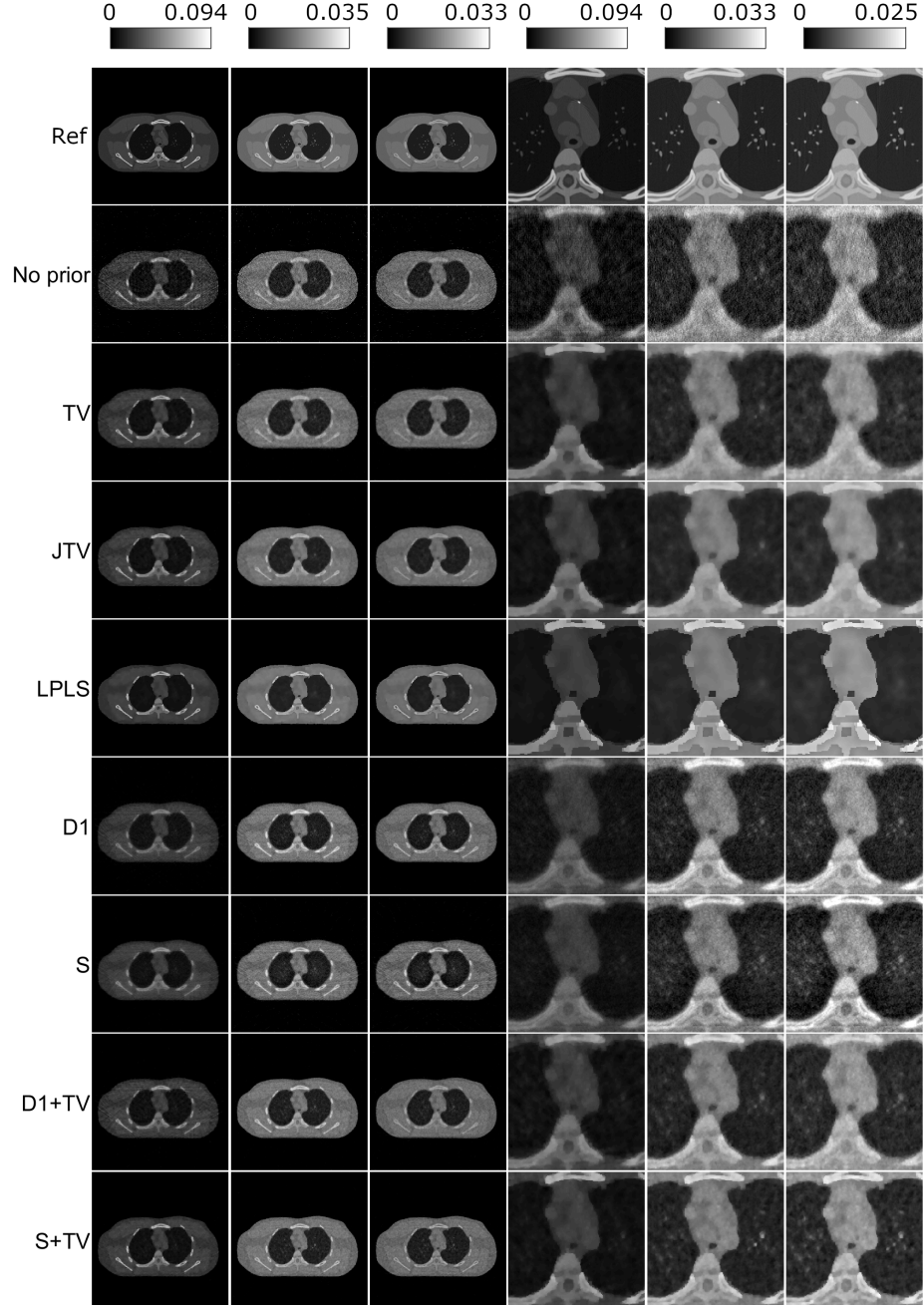


Figure 3: Reconstructed images for the simulation test case using 30 projection directions at each energy.

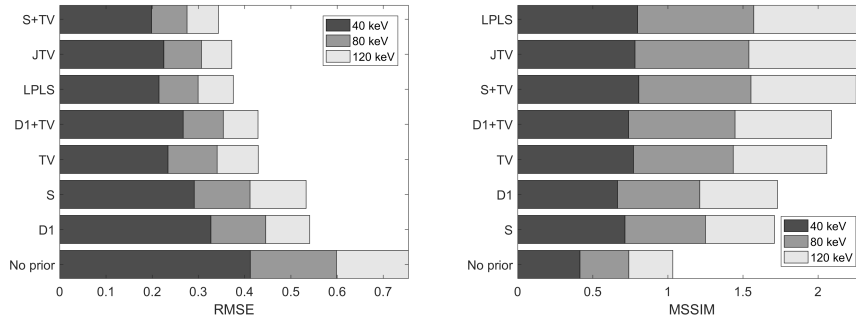


Figure 4: The RMS errors (left) and the mean SSIM indices (right) for the different reconstruction approaches using 30 projection directions at each energy.

see Fig 4. One interesting feature in the reconstructions is the difference in the amount of details in the reconstructions with the (JTV, LPLS) models compared to the reconstructions with the (D1, S) models. The JTV and LPLS models promote spatially piecewise regular solutions by posing different penalties for the sparsity of the image gradients. Consequently, the reconstructions lack some of the fine details but on the other hand have a very low level of spatial noise and very good RMSE and MSSIM metrics. In contrast, the reconstructions with the (D1, S) models show more details but are somewhat noisy, which is also reflected in the fact that the (D1, S) models have worse RMSE and MSSIM metrics than the (TV) model. This behavior is due to the fact that the (D1, S) models are based on promoting structural similarity in the energy direction without any penalty on spatial regularity. A good combination between the spatial details and noise level is reached when the (D1, S) models are used in combination with the TV regularization applied to each of the images for promoting spatial regularity (D1+TV, S+TV).

The results in Figures 3 and 4 reveal that the joint reconstruction models outperform the independent reconstruction models (No prior, TV) when using the same projection data of a total of 90 projection images. Figure 5 shows a comparison of TV and S+TV reconstructions using the same measurement data of 90 projection images with the 30+30+30 direction non-overlapping geometry that was used in Fig. 3 and also reconstructions using measurement data of 270 projection images using the same 90 directions for each energy. By comparison of the reconstructions S+TV (90) and TV (90), the S+TV outperforms the TV reconstructions also in this case when using classical overlapping projection geometry with the same 90 directions measured at each energy. More importantly, the comparison of TV(90) to S+TV(30W) reveals that the latter performs approximately equally well despite using only 90 projection images instead of 270. This finding suggests that the proposed combination of joint reconstruction and non-overlapping projection direction geometry can facilitate significant reduction of the x-ray dose.

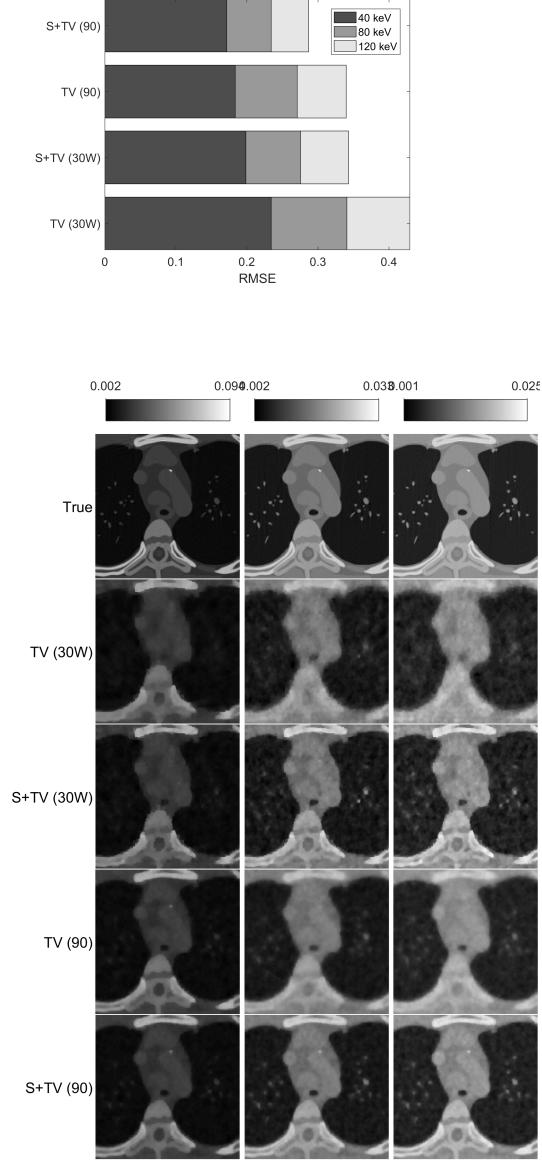


Figure 5: Comparison of TV and S+TV using 90 projection directions. Results labeled METHOD(90) are based on overall of $3 \times 90 = 270$ projection images using the same 90 directions for each energy. Results labeled METHOD(30W) are based on overall of 90 projections using the non-overlapping 30+30+30 directions (the same geometry that is used in Figure 3). Top section: Error metrics. Bottom section: ROI of the reconstructed images.

5.3 Experimental Data

The reconstructed images for the experimental data test case are shown in Figure 6. The first three columns show the reconstructions for E_1 , E_2 , and E_3 , respectively, and the next three columns show a region of interest from the corresponding reconstructions. For reference, the first row (Ref) shows ground truth reconstructions computed with the least squares (No prior) model using the full 720 projection angle data for each energy.

The reconstructions of the experimental data test case support the findings of the simulation test case. The joint reconstructions (JTV, LPLS, D1, S, D1+TV, S+TV) are visually better than the reference single energy reconstructions (No prior, TV) and there is a difference in the amount of details between (TV, JTV, LPLS) and (D1, S), visible for example from the outer edge of the target in the zoomed in images. The combined regularization approaches (D1+TV, S+TV) provide again a good combination of the spatial details and noise level, noticeable for example in the visibility of the two small low value areas on the right hand side of the zoomed in images.

6 Discussion and Conclusions

In this paper, we studied the performance of various structural similarity promoting joint reconstruction models using a novel low dose data acquisition protocol. The models were tested using both simulated and experimental measurement data and in both cases the linear parallel level sets (LPLS), joint total variation (JTV) and the combined structural similarity index based and total variation regularization (S+TV) performed the best. The regularization models that utilized only spectral regularization (S, D1) performed worse with respect to the RMSE and MSSIM fidelity metrics because they resulted in noisier reconstructions but nevertheless showed more details than the non-joint reconstruction approaches (No prior, TV). The combination of the joint reconstruction and the novel low dose projection protocol with non-overlapping projection directions was also compared to TV reconstructions using classical projection geometry, and was found to tolerate a clear reduction in the number of projection images, suggesting that the proposed approach can facilitate an effective way to reduce x-ray dose in multi-energy CT.

An implicit assumption in the proposed approach is that the target remains stationary during the imaging with different energies. However, with a data acquisition protocol that uses mutually non-overlapping projection angles and mid-scan energy switching, these motion issues should not, at least in theory, be any more problematic than with regular CT scanning. In addition, since the proposed combination of joint reconstruction and non-overlapping projection directions can operate on a smaller number of projection images than the combination of conventional projection geometries and reconstruction methods, it could potentially also facilitate a shorter overall scanning time to mitigate the risks of motion artifacts.

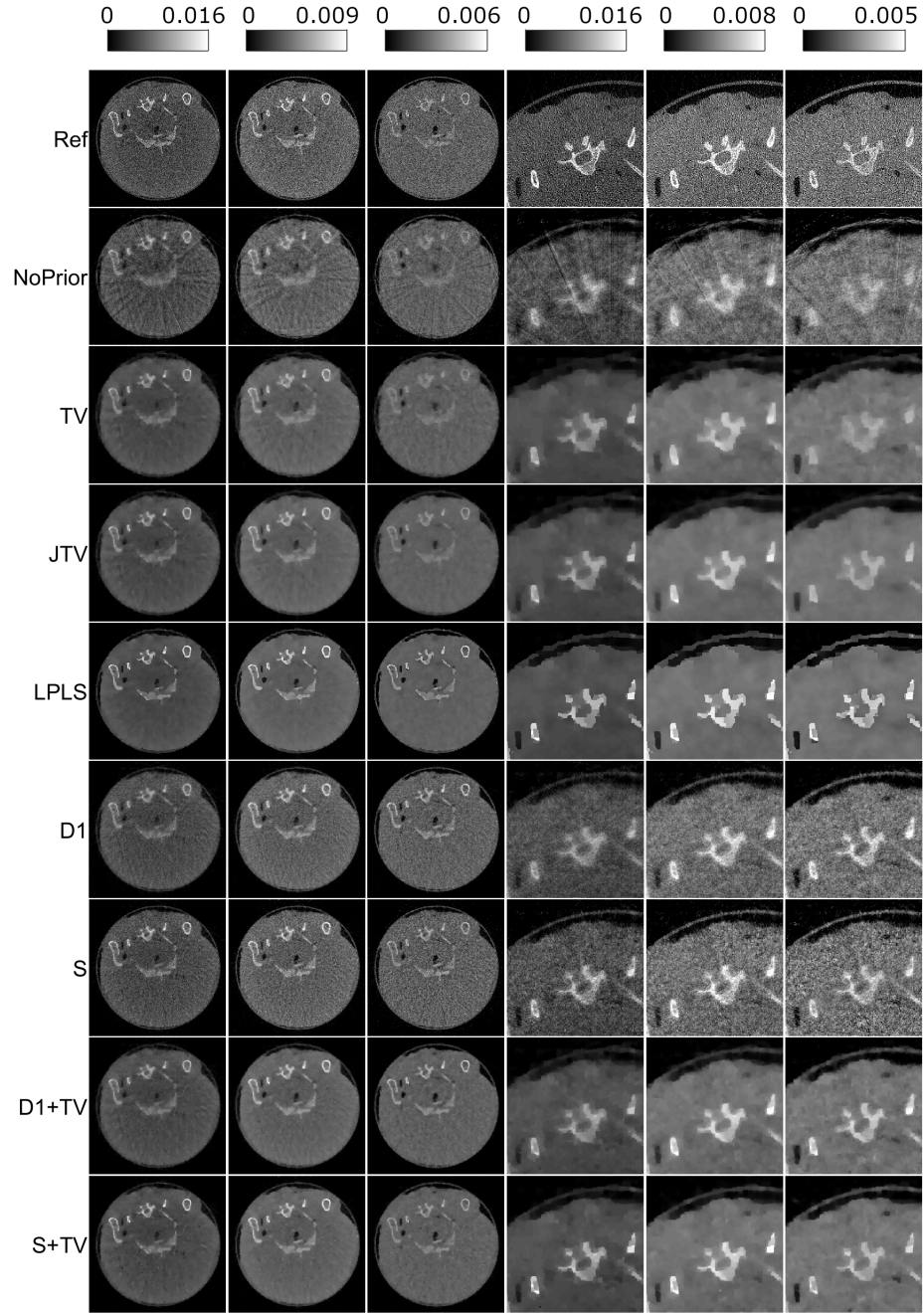


Figure 6: Reconstructed images for the experimental data test case.

Acknowledgments

This work was supported by the Academy of Finland (Project 312343, Finnish Centre of Excellence in Inverse Modelling and Imaging), the Jane and Aatos Erkko Foundation, and Business Finland project 6614/31/2016.

References

- [1] M. M. Lell, J. E. Wildberger, H. Alkadhi, J. Damilakis, and M. Kachelriess, “Evolution in computed tomography: The battle for speed and dose,” *Investigative Radiology*, vol. 50, no. 9, pp. 629–644, 2015.
- [2] L. De Chiffre, S. Carmignato, J.-P. Kruth, R. Schmitt, and A. Weckenmann, “Industrial applications of computed tomography,” *CIRP Annals - Manufacturing Technology*, vol. 64, p. 655–677, 2014.
- [3] C. H. McCollough, G. H. Chen, W. Kalender, S. Leng, E. Samei, K. Taguchi, G. Wang, L. Yu, and R. I. Pettrigrew, “Achieving routine submillisievert ct scanning: report from the summit on management of radiation dose in ct,” *Radiology*, vol. 264, no. 2, pp. 567–580, 2012.
- [4] D. T. Ginat and R. Gupta, “Advances in computed tomography imaging technology,” *Annual Review of Biomedical Engineering*, vol. 16, pp. 431–453, 2014.
- [5] C. H. McCollough, S. Leng, L. Yu, and J. G. Fletcher, “Dual-and multi-energy ct: principles, technical approaches, and clinical applications,” *Radiology*, vol. 276, no. 3, pp. 637–653, 2015.
- [6] H. W. Goo and J. M. Goo, “Dual-energy ct: New horizon in medical imaging,” *Korean Journal of Radiology*, vol. 18, no. 4, pp. 555–569, 2017.
- [7] J. Fornaro, S. Leschka, D. Hibbeln, A. Butler, N. Anderson, G. Pache, H. Scheffel, S. Wildermuth, H. Alkadhi, and P. Stolzmann, “Dual- and multi-energy ct: approach to functional imaging,” *Insights into Imaging*, vol. 2, no. 2, pp. 149–159, 2011.
- [8] R. Forghani and S. K. Mukherji, “Advanced dual-energy ct applications for the evaluation of the soft tissues of the neck,” *Clinical Radiology*, vol. 73, no. 1, pp. 70–80, 2018.
- [9] D. Marin, D. T. Boll, A. Mileto, and R. C. Nelson, “State of the art: Dual-energy ct of the abdomen,” *Radiology*, vol. 271, no. 2, pp. 327–342, 2014.
- [10] S. Nicolaou, T. Liang, D. T. Murphy, J. R. Korzan, H. Ouellette, and P. Munk, “Dual-energy ct: A promising new technique for assessment of the musculoskeletal system,” *American Journal of Roentgenology*, vol. 199, no. 5, pp. S78–S86, 2012.

- [11] W. D. Wong, S. Shah, N. Murray, F. Walstra, F. Khosa, and S. Savvas Nicolaou, “Advanced musculoskeletal applications of dual-energy computed tomography,” *Radiologic Clinics of North America*, vol. 56, no. 4, pp. 587–600, 2018.
- [12] L. Yu, S. Leng, and C. H. McCollough, “Dual-energy ct-based monochromatic imaging,” *American Journal of Roentgenology*, vol. 199, no. 5, pp. S9–S15, 2012.
- [13] A. A. Postma, P. A. M. Hofman, A. A. R. Stadler, R. J. van Oostenbrugge, M. P. M. Tijssen, and J. E. Wildberger, “Dual-energy ct of the brain and intracranial vessels,” *American Journal of Roentgenology*, vol. 199, no. 5, pp. S26–S33, 2012.
- [14] I. Danad, Z. A. Fayad, M. J. Willemink, and J. K. Min, “New applications of cardiac computed tomography,” *JACC: Cardiovascular Interventions*, vol. 8, no. 6, pp. 710–723, 2015.
- [15] K. Kalisz, S. Halliburton, S. Abbara, J. A. Leipsic, M. H. Albrecht, U. J. Schoepf, and P. Prabhakar Rajiah, “Update on cardiovascular applications of multienergy ct,” *RadioGraphics*, vol. 37, no. 7, pp. 1955–1974, 2017.
- [16] D. De Santis, M. Eid, C. N. De Cecco, B. E. Jacobs, M. H. Albrecht, A. Varga-Szemes, C. Tesche, D. Caruso, A. Laghi, and U. J. Schoepf, “Dual-energy computed tomography in cardiothoracic vascular imaging,” *Radiologic Clinics of North America*, vol. 56, no. 4, pp. 521–534, 2018.
- [17] R. Symons, B. Krauss, P. Sahbaee, T. Cork, M. N. Lakshmanan, D. A. Bluemke, and A. Pourmorteza, “Photon-counting ct for simultaneous imaging of multiple contrast agents in the abdomen: An in vivo study,” *Medical Physics*, vol. 44, no. 10, pp. 5120–5127, 2017.
- [18] R. E. Alvarez and A. Macovski, “Energy-selective reconstructions in x-ray computerised tomography,” *Physics in Medicine & Biology*, vol. 21, no. 5, pp. 733–744, 1976.
- [19] W. A. Kalender, “Dose in x-ray computed tomography,” *Physics in Medicine & Biology*, vol. 59, no. 3, pp. R129–R150, 2014.
- [20] M. Tubiana, L. E. Feinendegen, C. Yang, and J. M. Kaminski, “The linear no-threshold relationship is inconsistent with radiation biologic and experimental data,” *Radiology*, vol. 251, no. 1, pp. 13–22, 2009.
- [21] W. R. Hendee and M. K. O’Connor, “Radiation risks of medical imaging: Separating fact from fantasy,” *Radiology*, vol. 264, no. 2, pp. 312–321, 2012.
- [22] I. C. on Radiological Protection, “Icrp publication 103: The 2007 recommendations of the international commission on radiological protection,” *Annals of the ICRP*, vol. 37, no. 2–4, 2007.

- [23] I. C. on Radiological Protection, “Icrp publication 105: Radiological protection in medicine,” *Annals of the ICRP*, vol. 37, no. 6, 2007.
- [24] T. M. Buzug, *Computed Tomography: From Photon Statistics to Modern Cone-Beam CT*. Springer, 2008.
- [25] X. Pan, E. Y. Sidky, and M. Vannier, “Why do commercial ct scanners still employ traditional, filtered back-projection for image reconstruction?,” *Inverse Problems*, vol. 25, no. 12, p. 123009, 2009.
- [26] K. Hamalainen, A. Kallonen, V. Kolehmainen, M. Lassas, K. Niinimäki, and S. Siltanen, “Sparse tomography,” *SIAM Journal on Scientific Computing*, vol. 35, no. 3, pp. B644–B665, 2013.
- [27] D. S. Rigie and P. J. La Rivière, “Joint reconstruction of multi-channel, spectral ct data via constrained total nuclear variation minimization,” *Physics in Medicine & Biology*, vol. 60, no. 5, p. 1741–1762, 2015.
- [28] D. S. Rigie, A. A. Sanchez, and P. J. La Rivière, “Assessment of vectorial total variation penalties on realistic dual-energy ct data,” *Physics in Medicine & Biology*, vol. 62, no. 8, p. 3284–3298, 2017.
- [29] K. Kim, J. C. Ye, W. Worstell, J. Ouyang, Y. Rakvongthai, G. El Fakhri, and Q. Li, “Sparse-view spectral ct reconstruction using spectral patch-based low-rank penalty,” *IEEE Transactions on Medical Imaging*, vol. 34, no. 3, p. 748–760, 2015.
- [30] Y. Zhang, X. Mou, G. Wang, and H. Yu, “Tensor-based dictionary learning for spectral ct reconstruction,” *IEEE Transactions on Medical Imaging*, vol. 36, no. 1, pp. 142–154, 2017.
- [31] W. Wu, Y. Zhang, Q. Wang, F. Liu, P. Chen, and H. Yu, “Low-dose spectral ct reconstruction using image gradient ℓ_0 -norm and tensor dictionary,” *Applied Mathematical Modelling*, vol. 63, pp. 538–557, 2018.
- [32] D. Kazantsev, J. S. Jørgensen, M. S. Andersen, W. R. Lionheart, P. D. Lee, and P. J. Withers, “Joint image reconstruction method with correlative multi-channel prior for x-ray spectral computed tomography,” *Inverse Problems*, vol. 34, no. 6, p. 064001, 2018.
- [33] H. Gao, H. Yu, S. Osher, and G. Wang, “Multi-energy ct based on a prior rank, intensity and sparsity model (prism),” *Inverse Problems*, vol. 27, no. 11, p. 115012, 2011.
- [34] Q. Yang, W. Cong, and G. Wang, “Superiorization-based multi-energy ct image reconstruction,” *Inverse Problems*, vol. 33, no. 4, p. 044014, 2017.
- [35] O. Semerci, N. Hao, M. E. Kilmer, and E. L. Miller, “Tensor-based formulation and nuclear norm regularization for multienergy computed tomography,” *IEEE Transactions on Image Processing*, vol. 23, no. 4, pp. 1678–1693, 2014.

- [36] S. Niu, G. Yu, J. Ma, and J. Wang, “Nonlocal low-rank and sparse matrix decomposition for spectral ct reconstruction,” *Inverse Problems*, vol. 34, no. 2, p. 024003, 2018.
- [37] B. Chen, Z. Zhang, E. Y. Sidky, D. Xia, and X. Pan, “Image reconstruction and scan configurations enabled by optimization-based algorithms in multispectral ct,” *Physics in Medicine & Biology*, vol. 62, no. 22, pp. 8763–8793, 2017.
- [38] P. Blomgren and T. F. Chan, “Color tv: total variation methods for restoration of vector-valued images,” *IEEE transactions on image processing*, vol. 7, no. 3, pp. 304–309, 1998.
- [39] M. J. Ehrhardt and S. R. Arridge, “Vector-valued image processing by parallel level sets,” *IEEE Transactions on Image Processing*, vol. 23, no. 1, pp. 9–18, 2014.
- [40] Z. Wang, A. C. Bovik, H. R. Sheikh, and E. P. Simoncelli, “Image quality assessment: from error visibility to structural similarity,” *IEEE transactions on image processing*, vol. 13, no. 4, pp. 600–612, 2004.
- [41] M. H. McKetty, “The aapm/rsna physics tutorial for residents,” *Radiographics*, vol. 18, no. 1, pp. 151–163, 1998.
- [42] N. I. of Standards and T. P. M. Laboratory, “X-ray mass attenuation coefficients: Nist standard reference database 126,” 2004.
- [43] G. Poludniowski, G. Landry, F. DeBlois, P. M. Evans, and F. Verhaegen, “Spekcalc: a program to calculate photon spectra from tungsten anode x-ray tubes,” *Physics in Medicine and Biology*, vol. 54, pp. N433–N438, 2009.
- [44] F. Natterer, *The mathematics of computerized tomography*, vol. 32. Siam, 1986.
- [45] D. L. Donoho, “Compressed sensing,” *IEEE Transactions on Information Theory*, vol. 52, no. 4, pp. 1289–1306, 2006.
- [46] T. Bubba, M. März, Z. Purisha, M. Lassas, and S. Siltanen, “Shearlet-based regularization in sparse dynamic tomography,” in *Wavelets and Sparsity XVII*, vol. 10394, p. 103940Y, International Society for Optics and Photonics, 2017.
- [47] S. Siltanen, V. Kolehmainen, S. Järvenpää, J. Kaipio, P. Koistinen, M. Lassas, J. Pirttilä, and E. Somersalo, “Statistical inversion for medical x-ray tomography with few radiographs: I. general theory,” *Physics in Medicine & Biology*, vol. 48, no. 10, p. 1437, 2003.

- [48] V. Kolehmainen, S. Siltanen, S. Järvenpää, J. P. Kaipio, P. Koistinen, M. Lassas, J. Pirttilä, and E. Somersalo, “Statistical inversion for medical x-ray tomography with few radiographs: Ii. application to dental radiology,” *Physics in Medicine & Biology*, vol. 48, no. 10, p. 1465, 2003.
- [49] E. Y. Sidky and X. Pan, “Image reconstruction in circular cone-beam computed tomography by constrained, total-variation minimization,” *Physics in Medicine & Biology*, vol. 53, no. 17, p. 4777, 2008.
- [50] K. Hämäläinen, L. Harhanen, A. Hauptmann, A. Kallonen, E. Niemi, and S. Siltanen, “Total variation regularization for large-scale x-ray tomography,” *International Journal of Tomography & Simulation*, vol. 25, no. 1, pp. 1–25, 2014.
- [51] L. I. Rudin, S. Osher, and E. Fatemi, “Nonlinear total variation based noise removal algorithms,” *Physica D: nonlinear phenomena*, vol. 60, no. 1-4, pp. 259–268, 1992.
- [52] M. J. Ehrhardt, K. Thielemans, L. Pizarro, D. Atkinson, S. Ourselin, B. F. Hutton, and S. R. Arridge, “Joint reconstruction of pet-mri by exploiting structural similarity,” *Inverse Problems*, vol. 31, no. 1, p. 015001, 2014.
- [53] M. J. Ehrhardt, P. Markiewicz, M. Liljeroth, A. Barnes, V. Kolehmainen, J. S. Duncan, L. Pizarro, D. Atkinson, B. F. Hutton, S. Ourselin, *et al.*, “Pet reconstruction with an anatomical mri prior using parallel level sets,” *IEEE transactions on medical imaging*, vol. 35, no. 9, pp. 2189–2199, 2016.
- [54] Z. Wang and A. C. Bovik, “Mean squared error: Love it or leave it? a new look at signal fidelity measures,” *IEEE signal processing magazine*, vol. 26, no. 1, pp. 98–117, 2009.
- [55] W. P. Segars, M. Mahesh, T. J. Beck, E. C. Frey, and B. M. W. Tsui, “Realistic ct simulation using the 4d xcat phantom,” *Medical Physics*, vol. 35, no. 8, pp. 3800–3808, 2008.
- [56] W. P. Segars, G. M. Sturgeon, S. Mendonca, J. Grimes, and B. M. W. Tsui, “4d xcat phantom for multimodality imaging research,” *Medical Physics*, vol. 37, no. 9, pp. 4902–4915, 2010.
- [57] W. van Aarle, W. J. Palenstijn, J. Cant, E. Janssens, F. Bleichrodt, A. Dabrovolski, J. De Beenhouwer, K. J. Batenburg, and J. Sijbers, “Fast and flexible x-ray tomography using the astra toolbox,” *Optics express*, vol. 24, no. 22, pp. 25129–25147, 2016.
- [58] W. van Aarle, W. J. Palenstijn, J. De Beenhouwer, T. Altantzis, S. Bals, K. J. Batenburg, and J. Sijbers, “The astra toolbox: A platform for advanced algorithm development in electron tomography,” *Ultramicroscopy*, vol. 157, pp. 35–47, 2015.
- [59] “The ASTRA Toolbox.” <http://www.astra-toolbox.com/>.

- [60] E. Polak and G. Ribiere, “Note sur la convergence de méthodes de directions conjuguées,” *Revue française d’informatique et de recherche opérationnelle. Série rouge*, vol. 3, no. 16, pp. 35–43, 1969.